BIOCHEMISTRY
including biophysical chemistry & molecular biology

Article

pubs.acs.org/biochemistry

Analysis of Substrate Access to Active Sites in Bacterial Multicomponent Monooxygenase Hydroxylases: X-ray Crystal Structure of Xenon-Pressurized Phenol Hydroxylase from *Pseudomonas* sp. OX1

Michael S. McCormick and Stephen J. Lippard*

Department of Chemistry, Massachusetts Institute of Technology, Cambridge, Massachusetts 02139, United States

Supporting Information

ABSTRACT: In all structurally characterized bacterial multicomponent monooxygenase (BMM) hydroxylase proteins, a series of hydrophobic cavities in the α-subunit trace a conserved path from the protein exterior to the carboxylate-bridged diiron active site. This study examines these cavities as a potential route for transport of dioxygen to the active site by crystallographic characterization of a xenon-pressurized sample of the hydroxylase component of phenol hydroxylase from *Pseudomonas* sp. OX1. Computational analyses of the hydrophobic cavities in the hydroxylase α-subunits of phenol hydroxylase (PHH), soluble methane monooxygenase (MMOH), and toluene/*o*-xylene monooxygenase (ToMOH) are also presented. The results, together with previous findings from crystallographic studies of xenon-pressurized sMMO hydroxylase, clearly identify the propensity for these cavities to bind hydrophobic gas molecules in the protein interior. This proposed functional role is supported by recent stopped flow kinetic studies of ToMOH variants [Song, W. J., et al. (2011) *Proc. Natl. Acad. Sci. U.S.A. 108*, 14795−14800]. In addition to information about the Xe sites, the structure determination revealed significantly weakened binding of regulatory protein to the hydroxylase in comparison to that in the previously reported structure of PHH, as well as the presence of a newly identified metal-binding site in the α-subunit that adopts a linear coordination environment consistent with Cu(I), and a glycerol molecule bound to Fe1 in a fashion that is unique among hydrocarbon−diiron site adducts reported to date in BMM hydroxylase structures. Finally, a comparative analysis of the α-subunit structures of PHH, MMOH, and ToMOH details proposed routes for the other three BMM substrates, the hydrocarbon, electrons, and protons, comprising cavities, channels, hydrogen-bonding networks, and pores in the structures of their α-subunits.

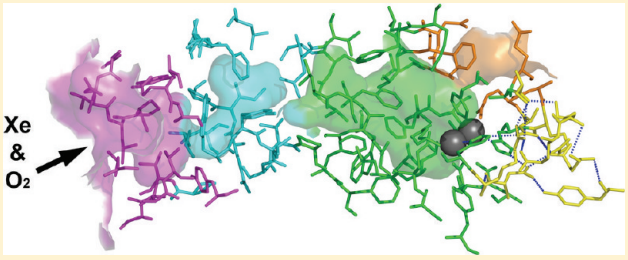

Phenol hydroxylase (PH) from *Pseudomonas* sp. OX1 belongs to a class of carboxylate-bridged non-heme diiron proteins known as bacterial multicomponent monooxygenases (BMMs) that convert hydrocarbons to alcohols and epoxides in nature.[1,2] These enzymes effect dioxygen activation and subsequent hydrocarbon substrate oxidation at diiron active sites located within hydrophobic pockets in the α-subunits of the 200−250 kDa heterodimeric, $(\alpha\beta\gamma)_2$, hydroxylase proteins.[2] The chemistry performed by BMMs endows their host bacteria with the ability to garner all of their carbon and energy needs from the oxidation of hydrocarbon substrates.[3] In addition to the hydroxylase, two or three accessory protein components participate in the process of substrate oxidation. An ∼38 kDa Fe_2S_2 reductase protein and a 10−15 kDa cofactor-less regulatory protein comprise the universal accessory proteins in BMMs, and an additional ∼10 kDa Rieske-type reductase assists in shuttling electrons to the hydroxylase in the four-component BMM systems.[2]

The hydroxylase protein components of soluble methane monooxygenase (sMMO) from *Methylococcus capsulatus* (Bath)[4−11] and *Methylosinus trichosporium* OB3b[12] (MMOH), toluene 4-monooxygenase (T4MO) from *Pseudomonas mendocina* KR1[13] (T4MOH), and toluene/*o*-xylene monooxygenase (ToMO) from *Pseudomonas* sp. OX1[14,15] (ToMOH) have been characterized by X-ray crystallography. In addition, hydroxylase−regulatory protein complexes have been crystallographically characterized from the PH (PHH−PHM) and T4MO (T4MOH−T4MOD) systems from *Pseudomonas* sp. OX1[16] and *P. mendocina* KR1,[13] respectively. The diiron active site coordination and geometry, as well as the sequence and many of the relative orientations of surrounding residues, are highly maintained within the BMM family. They are also similar to those in other carboxylate-bridged diiron proteins, including the functionally divergent enzymes ribonucleotide reductase R2 subunit,[17] ferritin,[18] and steroyl-acyl carrier protein Δ^9-desaturase.[19] Reactivity toward hydrocarbons distinguishes the BMM class among diiron carboxylate enzymes by the structure

Received: August 9, 2011
Revised: November 13, 2011
Published: December 2, 2011

ACS Publications © 2011 American Chemical Society

of the protein scaffold and the nature of oxygenated active site intermediates generated during catalysis.

Catalytic hydrocarbon oxidation in BMMs requires four substrates, hydrocarbons, molecular oxygen, electrons, and protons in the form of H_3O^+ cations, and yields two products, water and the hydroxylated or epoxidized hydrocarbon substrate.[20] Understanding the means by which the BMM hydroxylase scaffolds facilitate and control the movement of substrates and products to and from the diiron active site during catalysis, while simultaneously binding to and dissociating from the accessory proteins, is key in characterizing the mechanisms by which these systems operate. Structural and mechanistic studies of BMMs indicate that specific features and individual residues in the hydroxylase protein structures, which are often conserved in BMMs and diiron carboxylate proteins in general, function to transport substrate to the diiron centers in these systems.[2,20] Such findings include hydrocarbon substrate−hydroxylase complex crystal structures of MMOH[7,10,11] and ToMOH[15] that reveal substrate or substrate analogues bound in their respective active sites and surface-linked pockets or channels in the protein interior. Similar results have been observed in Δ9D,[19] the surface-to-active site channels in which are analogous to those in ToMOH[14,15] and T4MOH.[19]

The diiron active sites in BMM hydroxylases are located in their α-subunits, approximately 12 Å below the protein surface adjacent to a hydrophobic pocket formed primarily by the iron-ligating four-helix bundle (Figure 1).[2] A neighboring space

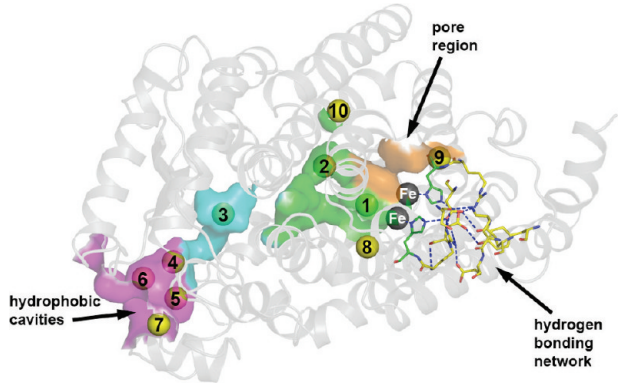

Figure 1. Xenon binding in the α-subuint of Xe-PHH. Proposed substrate access pathways that are common to all structurally characterized BMMs are labeled with arrows. van der Waals surfaces of the hydrophobic cavities and pore region are colored magenta (cavity 3), cyan (cavity 2), green (cavity 1), and orange (pore region). The putative electron-transport hydrogen-bonding network residues are shown as yellow sticks. Iron and xenon atoms are represented as dark gray spheres and yellow spheres, respectively. The α-subunit protein backbone is shown as light gray ribbons.

defines a structural pore region that separates the active site pocket from the protein exterior by only a few highly conserved residues on the surface of the α-subunit.[2,20] The presence of this short pathway to the diiron center from the protein exterior was noted in early structures of MMOH[4,5] and later analyzed in more detail in product-bound structures of the hydroxylase.[7] Nearly identical pore regions were subsequently observed in ToMOH[14] and T4MOH.[13] An analogous pathway was also observed in the first structure of PHH as completely solvent exposed in the absence of bound regulatory protein and occluded in the hydroxylase−regulatory protein complex.[16]

In addition to these findings about the pore region, the size, conformation, and solvent accessibility of the active site pocket are known to undergo changes upon reduction of the active site metal ions[8,9,14] and in the presence of bound products and product analogues.[7,10] Also common to the BMM hydroxylase structures is a series of hydrophobic cavities that extends from openings at the surface, approximately 35 Å from the diiron center, and passes through the α-subunit to the active site pocket (Figure 1).[21] Similar to the pore region, the presence of these cavities and their potential role in substrate transport were first noted in structures of MMOH,[4,5,7,10,11] and analogous hydrophobic cavities were subsequently observed in structures of ToMOH,[14] PHH,[16] and T4MOH.[13] The pore and hydrophobic cavity pathways that are common to all structurally characterized BMM hydroxylases are indicated in Figure 1 in the context of the present Xe-PHH structure. The conserved hydrogen-bonding network that represents a putative electron-transport pathway in BMMs[2,15,16,20] is also depicted, along with the 10 xenon atoms located in the α-subunit of Xe-PHH. Note that the color scheme used in this figure is maintained throughout this article. Structures of hydroxylases from the four-component systems ToMO[14,15] and T4MO[13] have revealed the presence of a wide channel that provides an additional 35 Å route to the diiron center, delineating a pathway that differs from that defined by the hydrophobic cavities and exposes the active site cavity to bulk solvent via an opening adjacent to the pore region. Crystallographic characterization of the hydroxylase−regulatory protein complex from the T4MO system reveals that this channel becomes inaccessible to small molecules upon formation of the complex with the regulatory protein.[13]

In this study, we investigated the series of conserved hydrophobic cavities in the PH hydroxylase (Figure 1) as a potential route for transfer of dioxygen to the diiron center during catalysis. The approach, which is complementary to our recent kinetic investigations of the O_2-transport pathway in variants of ToMOH,[22] involved determination of the X-ray structure of a xenon-pressurized PHH crystal to test the through-cavities hypothesis for dioxygen transport in BMMs. Xenon is an ideal gas to use for probing dioxygen binding sites in protein crystallography, because it is quite similar to molecular oxygen in size, hydrophobicity, and polarizability (Table S1 of the Supporting Information).[23] Unlike molecular oxygen, however, xenon has 54 electrons, which render it highly visible in difference Fourier electron density maps. The results, together with comparative analyses of proposed substrate-transport routes in PHH, MMOH, and ToMOH, from computational studies of BMM α-subunits using *PyMOL*[24] and *CAVER*,[25] provide new detail regarding the conservation and unique features of the individual pathways across the BMM family and suggest specific roles for each one.

MATERIALS AND METHODS

General Considerations. PHH was expressed as described previously.[1] The iron content was measured by a FerroZine assay[26] and enzyme activity by a coupled colorimetric assay using catechol 2,3-dioxygenase as previously described.[1] The PHH sample for crystallization and subsequent Xe pressurization studies contained 3.6 Fe atoms/dimer and exhibited an enzymatic activity of 470 ± 40 milliunits mg^{-1}. The regulatory protein, PHM, was expressed and purified as described previously.[27]

Crystallization, Xenon Pressurization, and X-ray Diffraction Data Collection. PHH crystals were grown by the hanging drop vapor diffusion method at 18 °C using previously published conditions,[16] with modifications as described below. Protein solutions contained 35 μM PHH and 28 μM phenol hydroxylase regulatory protein (PHM) in 10 mM MES (pH 7.1) and 10% (v/v) glycerol. The precipitant solution contained 150 mM $Na_2MoO_4 \cdot 2H_2O$, 100 mM Tris-HCl (pH 7.0), 5% (v/v) glycerol, and 17−25% PEG 8000 (w/v) and was prepared individually for each well in the crystallization tray from concentrated stocks of the solution components. After preparation of the precipitant solutions, the 24-well tray was incubated at 4 °C and shaken for approximately 15 min before addition of the hanging drops and cover slides. This step was required for proper mixing of the precipitant components because of the high solution viscosity. Hanging drops contained 2 μL of protein solution combined with 2 μL of precipitant solution. Cryogenic solutions for data collection combined the precipitant solution with glycerol (20%, v/v).

Crystalline samples of PHH were shipped to Stanford Synchrotron Radiation Laboratory (SSRL) at ambient temperature in a tube containing 500 μL of cryo solution. Many of these crystalline samples were individually subjected to xenon pressurization. At ambient temperature, single crystals were mounted on cryo loops that were subsequently placed in the gas pressurization cell[28] along with 500 μL of distilled water to prevent crystal dehydration. Samples were then pressurized with 2.1×10^6 Pa xenon gas for 2−15 min before the pressure was released and the crystals immediately frozen in liquid nitrogen. After being frozen, the crystals were transferred to the Stanford Automated Mounting robot cassette[29] and screened for diffraction quality.

X-ray diffraction data were collected at SSRL on beamline 9-2 using the *Blu-Ice* data collection suite.[30] Crystal annealing was conducted as described for the 1.85 Å native ToMOH structure determination;[14] however, different annealing times were investigated, ranging from 1 to 10 s, at 1 s intervals. Diffraction data were integrated and scaled in *HKL2000*.[31]

Structure Determination and Refinement. Molecular replacement phasing of the xenon PHH−PHM data was accomplished by using *EPMR*[32] and 2.3 Å resolution native PHH−PHM complex coordinates [Protein Data Bank (PDB) entry 2INP][16] in which all non-protein atoms and the side chains of the iron coordinating ligands had been removed from the starting model. Phasing was additionally conducted using the model described above lacking the coordinates for PHM. After phasing, subsequent models were built in *Coot*[33] and refined by *REFMAC5*[34] in *CCP4*.[35] PHM and Xe atom occupancies as well as simulated annealing composite omit maps were calculated in *CNS*.[36] Xenon atoms were located by manually fitting them into high-sigma ($\geq 8.0\sigma$) peaks in the simulated annealing composite omit $2F_o - F_c$ electron density map. PHM molecule and Xe atom occupancy refinements were performed by fixing the *B* factors of the refined atoms to the average value for the α-, β-, and γ-subunits. MSDchem ideal coordinates as well as *CNS* topology and parameter files for glycerol, HEPES, and MOPS heterocompounds were obtained from the HIC-UP database (residue codes GOL, HPE, and MPO, respectively).[37]

***PyMOL* Analysis of Pockets in BMM Hydroxylases.** The macromolecular structure visualization program *PyMOL* provides accurate representations of van der Waals surfaces.[24] Utilizing this feature, prominent pockets in the crystallographically characterized BMM hydroxylases can be readily defined. With this information, each protein residue that contributes to the surface of the various BMM hydroxylase pockets was identified. Results reported here were obtained from analysis of 1.95 Å resolution Xe-PHH (this work), 1.70 Å resolution MMOH from *M. capsulatus* (Bath) (PDB entry 1MTY), and 1.85 Å resolution ToMOH (PDB entry 2INC).

BMM Hydroxylase α-Subunit Protein Sequence Alignments. Protein sequence alignments for analyzing hydroxylase α-subunit residue conservation were performed using *ClustalW*.[38] The protein sequences of PHH and ToMOH from *Pseudomonas* sp. OX1 (European Molecular Biology Laboratory accession codes AAO47358 and CAA06654, respectively), MMOH from *M. capsulatus* (Bath) (AAB62392), T4MOH from *P. mendocina* KR1 (AAS66660), alkene monooxygenase expoxidase from *Rhodococcus* sp. RHA1 (YP700435), and butane monooxygease hydroxylase from *Pseudomonas butanovora* (AAM19727) were used for the sequence alignments.

***CAVER* Analysis of BMM Hydroxylase Pockets.** The *CAVER* software package facilitates the identification of routes leading from cavities in the interior of proteins to bulk solvent outside the protein matrix, via a reciprocal distance search algorithm.[25] Data output from *CAVER* includes the cross section diameter of all calculated pathways at multiple points along their trajectories, allowing for the identification of both the location and size of points of interest along each pathway. The starting point for each substrate access pathway search in this study was the midpoint of the active site cavity, which was manually chosen on the basis of van der Waals surface calculations initially conducted in *PyMOL* (vide supra).[24] *CAVER* parameters were set to compute 10 independent pathways from the starting position to the protein exterior via available space in the structure interior. Each of 10 calculated pathways was output as coordinates spaced at 0.8 Å intervals along the trajectory. Trajectory coordinates contain precise radii, allowing for accurate relative width measurements along the pathways. Structures of 1.70 Å resolution MMOH from *M. capsulatus* (PDB entry 1MTY), 2.15 Å resolution ToMOH (PDB entry 1T0Q), and the 2.70 Å resolution PHH−PHM complex (PDB entry 2INN) were subjected to *CAVER* analysis with these parameters, following deletion of all non-protein atoms from the structure coordinate list. In the case of the PH analysis, the protomer not bound to PHM in the PHH−PHM structure, hereafter termed protomer A, was chosen to represent PHH in the absence of PHM. Conversely, the protomer bound to PHM, hereafter termed protomer B, was analyzed for information about PHH in the presence of bound regulatory protein.

RESULTS AND DISCUSSION

Crystallization, Xenon Pressurization, and Data Collection. PHH crystals formed in 2−3 days. Among crystals subjected to xenon pressurization and diffraction screening, the best quality data came from one that crystallized from 150 mM $Na_2MoO_4 \cdot 2H_2O$, 100 mM Tris-HCl (pH 7.0), 5% (v/v) glycerol, and 19% PEG 8000 (w/v), was pressurized with xenon for 5 min, and was subjected to a 2 s annealing time. Diffraction data collection statistics are reported in Table 1.

Structure Determination and Coordinate Refinement. Global folds for the α-, β-, and γ-subunits of the Xe-PHH dimer (Figure S1 of the Supporting Information) are

Table 1. X-ray Data Collection and Refinement Statistics for Xe-PHH

	Xe-PHH
Data Collection	
Beamline	SSRL 9-2
Wavelength (Å)	0.979
Space Group	$P2_12_12_1$
Unit cell dimensions (Å)	83.9 × 141.8 × 181.2
Resolution range (Å)	38.0−1.95
Total Reflections	138448
Unique Reflections	94048
Completeness (%)[a]	92.5 (82.1)
$I/\sigma(I)$[a,b]	21.0 (2.2)
R_{sym} (%)[a]	6.7 (53.5)
Refinement	
R_{cryst} (%)[c]	18.3
R_{free} (%)[d]	22.8
Average *B*-value (Å^2)	28.6
RMSD bond length (Å)	0.018
RMSD bond angles (°)	1.70
Number of Atoms/Molecules[e]	
Protein[e]	15336 (29.1)
Non-Protien[e]	709 (39.8)
Iron[e]	4 (38.8)
Zinc[e]	2 (22.8)
Copper[e]	2 (34.8)
Xenon[e]	24 (37.6)
Water[e]	588 (38.6)
Glycerol[e]	10 (42.9)
MOPS[e]	1 (70.2)
HEPES[e]	1 (67.3)

[a]Values in parentheses are for the highest resolution shell. [b]$R_{sym} = \sum_i\sum_{hkl}|I_i(hkl) - \langle I(hkl)\rangle|/\sum_{hkl}\langle I(hkl)\rangle$, where $I_i(hkl)$ is the *i*th measured diffraction intensity and $\langle I(hkl)\rangle$ is the mean intensity for the Miller index (*hkl*). [c]$R_{cryst} = \sum_{hkl}||F_o(hkl)| - |F_c(hkl)||/\sum_{hkl}|F_o(hkl)|$. [d]$R_{free} = R_{cryst}$ for a test set of reflections (5% in each case). [e]Values in parentheses are for the average *B*-factor, in Å^2, for the atoms or molecules listed.

essentially identical to that for the hydroxylase component of the previously reported PHH−PHM structure,[16] with the exception of the conformational changes observed for helices E and F in the protomer B α-subunit (vide infra). Structural alignments with the PHH−PHM coordinates indicate C_α-to-C_α root-mean-square deviations of 0.74 Å for the hydroxylase and 0.26 Å for the protomer B α-subunit alone. Refinement statistics for Xe-PHH are reported in Table 1.

There Is Little Regulatory Protein Binding to the Hydroxylase in This Structure. Formation of the hydroxylase−regulatory protein complex is required during BMM catalysis[27,39] and causes structural changes in the vicinity of the diiron center and reductase protein-binding surface of the hydroxylase that are discussed elsewhere.[2,16,20] The previously reported structure of PHH contained the PHM regulatory protein bound to protomer B with an estimated 40−50% occupancy and with zero occupancy on protomer A.[16] Protein used in this work was isolated and purified from the same cell extracts, and it crystallized in the same space group determined in the previous PHH−PHM structure analysis to yield isomorphous crystals. The Xe-PHH data were therefore phased by molecular replacement using the hydroxylase−regulatory protein complex. The resulting $2F_o - F_c$ composite omit maps in the case of Xe-PHH, however, indicated significantly less electron density at the PHM binding site than in that of the previously reported PHH−PHM complex. It was therefore quite difficult to model bound PHM into the electron density of the Xe-PHH structure, and attempts to do so consistently resulted in poor protein backbone and side chain geometry for the regulatory protein, even after multiple rounds of model fitting and refinement. The final refinements were therefore conducted with complete omission of the regulatory protein, which afforded statistics that were significantly better than those obtained with the regulatory protein present. The refined dimensions of the hydroxylase-only Xe-PHH unit cell are notably smaller than those of the PHH−PHM complex and result in a 12% decrease in unit cell volume with respect to that of the regulatory protein-containing structure. The difference in unit cell volume reflects the lack of partial PHM occupancy for Xe-PHH. Moreover, detailed inspection of the fully refined Xe-PHH α-subunits revealed that the model exhibited virtually none of the structural features attributed to regulatory protein binding in the X-ray structures of PHH−PHM[16] and T4MOH−T4MOD[13] complexes. Most significant were the conformations of the iron-ligating α-subunit helices E and F compared to those of the BMM hydroxylase−regulatory protein complex structures. In the PHH−PHM and T4MOH−T4MOD complexes, the π-helical region of the regulatory protein-bound α-subunit helix E is extended, an effect ascribed to regulatory protein binding. Shifts in the position of α-subunit helix F were also noted in the PHH−PHM structure. In the structure of Xe-PHH, however, no such alterations in the E or F helices occurred for either protomer. We therefore conclude that any effects of PHM binding in the Xe-PHH structure are marginal at best, and we proceeded in our analysis without PHM coordinates included in the structure model.

Metal Binding in Xe-PHH. The diiron centers in Xe-PHH (Figure S2 of the Supporting Information) have metrical parameters similar to those of the PHH−PHM complex[16] and resemble that of mixed-valent MMOH.[9] There is a notable absence of solvent-derived ligands bound to the iron atoms. In the Xe-PHH structure, however, there is evidence of a presumably deprotonated glycerol molecule bound exclusively to Fe1 in both protomers and in place of a terminal water molecule on Fe1 that was located in the previous structure.[16] The glycerol assignment is supported by the $2F_o - F_c$ composite omit electron density (Figure S3 of the Supporting Information). The resulting hydrocarbon coordination mode is unlike that encountered previously in any BMM hydroxylase. All prior structures of alcohol-bound BMM hydroxylases contained an asymmetrically bridged hydrocarbon.[7,11,15] The significance of this finding with respect to substrate binding to the enzyme is unclear at present.

The Xe-PHH structure contains a presumed structural zinc site in the α-subunit near its interface with the β-subunit (Figures S4 and S5 of the Supporting Information). As in the previously reported PHH−PHM structure,[16] the zinc atom is in a nearly perfect tetrahedral environment composed of four cysteine sulfur atoms with 2.2−2.4 Å Zn−S bond distances that are typical for such units.

In addition to the diiron and zinc sites in Xe-PHH, we could identify a third metal-binding site in the structure, at the surface of the α-subunit near the dimer interface (Figure S6 of the Supporting Information). This single-atom binding site appears from the electron density to consist of a transition metal bound by two histidine imidazole ligands coordinated in a nearly linear

fashion. In both protomers, the M−N distances are 2.1 and 2.0 Å for the δ- and ε-nitrogens, respectively. No additional ligands to this metal are observed in the electron density. The linear coordination geometry would be consistent with Cu(I),[40,41] but we have no evidence to support that assignment. It is unknown whether this surface-bound metal ion could have a function, although we note that the expression of sMMOH in BMMs requires low copper concentrations. The metal is most likely a consequence of an impurity in one of the protein purification or crystallization reagents, from which no attempt was made to exclude copper.

Xenon Atom-Binding Sites in Xe-PHH. Twenty-four xenon atoms, 12 in each protomer, were located in the structure (Figure S1 of the Supporting Information), including 14 in the MMOH-like hydrophobic cavities (Table S2 of the Supporting Information and Figure 1). Their refined occupancies range from 0.3 to 1.0, with an average of 0.8 (Table S2). In cases where the occupancy refined to a value greater than or equal to unity, it was subsequently fixed at 1.0 and the *B* factor was allowed to be refined. Magnified images of the 10 xenon-binding sites located in the α-subunit of Xe-PHH protomer B are shown in Figure 2. Distances between the xenon atoms in the hydrophobic cavities and the active site iron atoms are listed in Table S3 of the Supporting Information.

As is typical for a xenon-bound protein structure,[42] most of the residues that comprise the various binding sites have hydrophobic side chains and are positioned 3.5−4.5 Å from the bound xenon atom (Table S2 and Figure 2). A notable trend in the occupancies of the xenon atoms bound to the hydrophobic cavities is a significant decrease with increasing proximity to the buried diiron center (Table S2). Because Xe presumably enters the cavities from the protein exterior, this trend is that expected in the absence of a driving force, such as O_2 consumption, toward the active site. Possibly relevant is the lack of ordered water molecules observed at or near the xenon-binding sites in the structure of PHH lacking exposure to pressurized xenon.[16]

Cavities, Channels, and Pores in BMM Hydroxylase α-Subunits. To compare the pathway through the PHH α-subunit to the active site as delineated by the Xe atoms in our structure determination with potentially analogous routes through other BMM hydroxylases, all residues contributing to the van der Waals surfaces of open spaces in the α-subunits of PHH, MMOH, and ToMOH were identified by using *PyMOL*.[24] The figures summarizing this analysis reveal that the three hydrophobic cavities, as well as the pore region, are spatially well-defined in the α-subunits of PHH (Figure 3), MMOH (Figure 4), and ToMOH (Figure 5). Also apparent in the images is conservation of the relative orientations of the cavity and pore access pathways with respect to the diiron center (gray spheres) and putative electron-transfer hydrogen-bonding network (yellow residues).[2,15,16,20] A large majority of the residues contributing to the interior surfaces of the cavities, as labeled in the figures, are hydrophobic, with few polar side chains facing inward.

Comparison of individual cavities 1 (green), 2 (cyan), and 3 (magenta) in the three hydroxylase proteins indicates that (1) cavity 1 is considerably larger in PHH than in MMOH or ToMOH (Figures 3−5, green), (2) cavity 2 is similarly sized and isolated from cavities 1 and 3 in all three hydroxylases (Figures 3−5, cyan), and (3) cavity 3 is largest in MMOH and solvent-restricted whereas in PHH and ToMOH it is smaller but solvent-accessible (Figures 3−5, magenta). The fact that the structures and hydrophobicity of these cavities are conserved without strict conservation of the contributing residues, together with the fact that they bind xenon in MMOH[10] and PHH, is consistent with their postulated function in dioxygen transport in all three BMM systems[14,22] and possibly for methane transport in MMOH.[4,5] This theory is further supported by a recent site-directed mutagenesis study of ToMOH in which dioxygen migration rate constants are diminished or increased in mutants with modified cavity sizes.[22]

A comparison of the pore regions (Figures 3−5, orange) reveals that the residues contributing to its surface are relatively polar and highly conserved with respect to those constituting the other pockets. Specifically, the pore access pathway in all three hydroxylases includes a strictly conserved active site pocket threonine (PHH T203, MMOH T213, and ToMOH T201) that is required for catalysis,[43] a strictly conserved surface asparagine (PHH N204, MMOH N214, and ToMOH N202) that undergoes a rotamer shift upon reduction of the active site metal ions in MMOH[8,9] and ToMOH[14] and forms a hydrogen-bonding interaction with the regulatory protein in the PHH−PHM complex,[16] and conserved surface glutamine/glutamate (PHH Q230, MMOH E240, and ToMOH Q228) and iron-ligating glutamate (PHH E233, MMOH E243, and ToMOH E231) residues that also change conformation upon reduction of the active site in MMOH[8,9] and ToMOH[14] (Figure 6). In all cases, the remaining residues that contribute to the pocket space are hydrophobic. The fact that conserved and conformationally flexible residues contribute to the pore surface suggests that redox activity at the active site is linked to its accessibility during catalysis. These observations suggest that the function of the pore may be to effect the translocation of protons into the BMM hydroxylase active site cavity as required for proton-coupled electron transfer[20] and/or dioxygen activation.[43−45] In the case of PHH, its relatively large and open pore (Figure 6) may also facilitate substrate access and product egress, given the absence of a ToMOH-like channel.[15,16] Such a polar substrate access route is expected in PHH because of its preference for phenolic substrates.[1]

The channel in ToMOH (Figure 5, gray) abuts cavities 1 and 2 and then extends toward the protein surface. This channel closes down upon binding of the regulatory protein, as indicated by a structural study of the hydroxylase−regulatory protein complex characterized in the cognate toluene-4-monooxygenase system.[13] A comparison of the analogous region of the α-subunit in PHH reveals that it is somewhat conserved and contributes to a relatively large cavity 1 in PHH (Figure 3, green). In MMOH (Figure 4), we also do not find a channel-like space in the analogous region of its α-subunit but instead identify hydrophobic amino acid side chains, including those of F188, F236, and L110, projecting into the area to prevent the formation of one. These observations about the channel in the context of the substrate specificities of PHH, ToMOH, and MMOH suggest that it may have evolved in four component hydroxylase systems to accommodate more polar hydrocarbon substrates, but not in the other two systems to limit active site solvent access and thus protect the integrity of higher-energy intermediates formed during dioxygen activation.[22,43−45] As mentioned above, the channel is closed upon formation of the complex with the regulatory protein in T4MO.[13]

Sequence alignment of various BMM α-subunits, summarized in Figure S7 of the Supporting Information, indicates

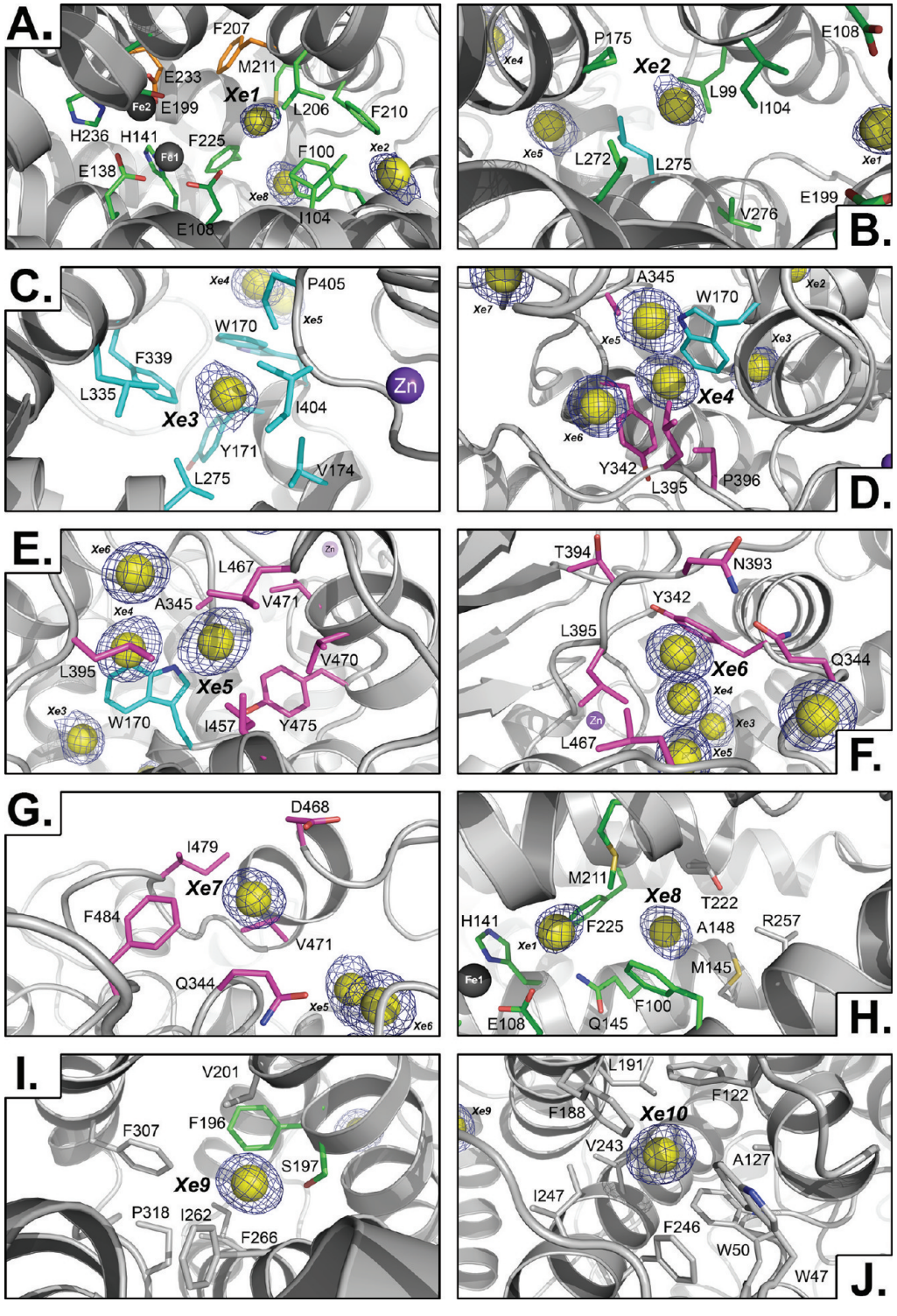

Figure 2. Detailed views of xenon-binding sites in the α-subunit of Xe-PHH. Xenon (yellow), iron (dark gray), and zinc (purple) atoms are shown as spheres. Residues within 5 Å of xenon atoms are shown as sticks and colored according to the scheme used in Figure 1 if they contribute to the van der Waals surface of the hydrophobic cavities or pore region and colored light gray if they do not. Composite omit electron density contoured to 5.0σ is colored dark blue. The protein backbone is depicted as light gray ribbons. Xenon sites 1−10 are depicted (A−J, respectively).

conservation in the hydrophobicity of residues contributing to the xenon-binding sites in Xe-PHH, suggesting that similar hydrophobic pockets capable of binding xenon, as a surrogate for dioxygen, are present within hydroxylases throughout the entire enzyme class. Mutagenesis studies of the ToMOH system strongly support this conclusion.[22]

***CAVER* Analysis of BMM Hydroxylase Pockets.** Substrate access calculations with *CAVER*[25] for the PHH−PHM structure[16] reveal that (1) there are three potential routes of molecular access from the protein surface to the diiron center in the α-subunit of PHH, (2) the route exhibiting the largest cross section is the pore region, which changes in length

dx.doi.org/10.1021/bi201248b | *Biochemistry* 2011, 50, 11058−11069

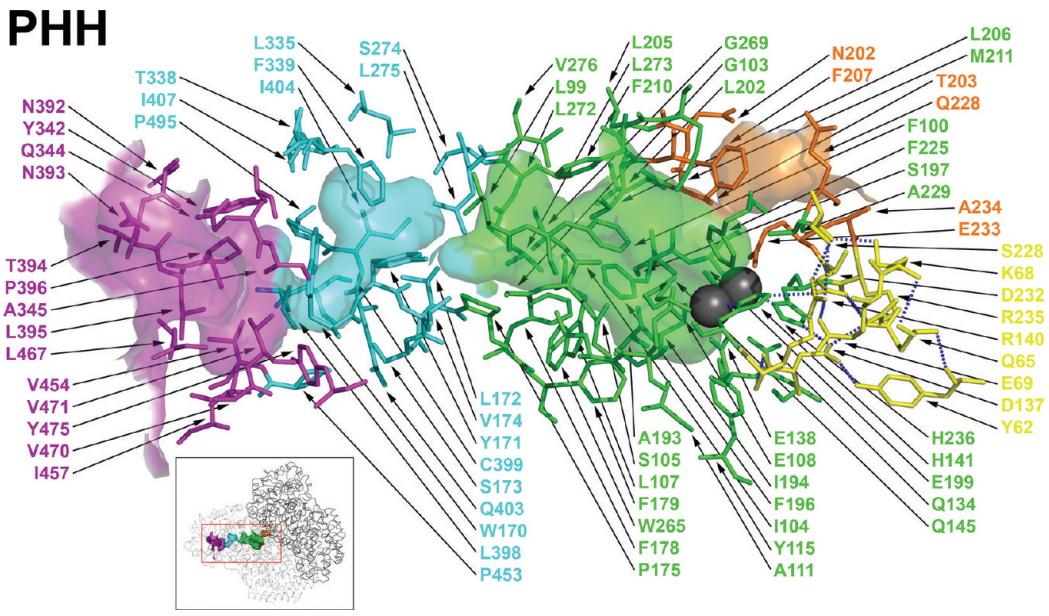

Figure 3. Surface-to-active site pockets in the α-subuint of PHH. Hydrophobic cavities and pore region pockets are represented as van der Waals surfaces colored magenta (cavity 3), cyan (cavity 2), green (cavity 1), and orange (pore region). Protein residues that contribute to the van der Waals surface are shown as sticks using the same color scheme used for the surface representations. The putative electron-transport hydrogen-bonding network residues are shown as yellow sticks. Iron atoms are represented as dark gray spheres. The inset indicates the orientation of the hydroxylase dimer protomers A (dark ribbons) and B (light ribbons) depicted in the primary figure.

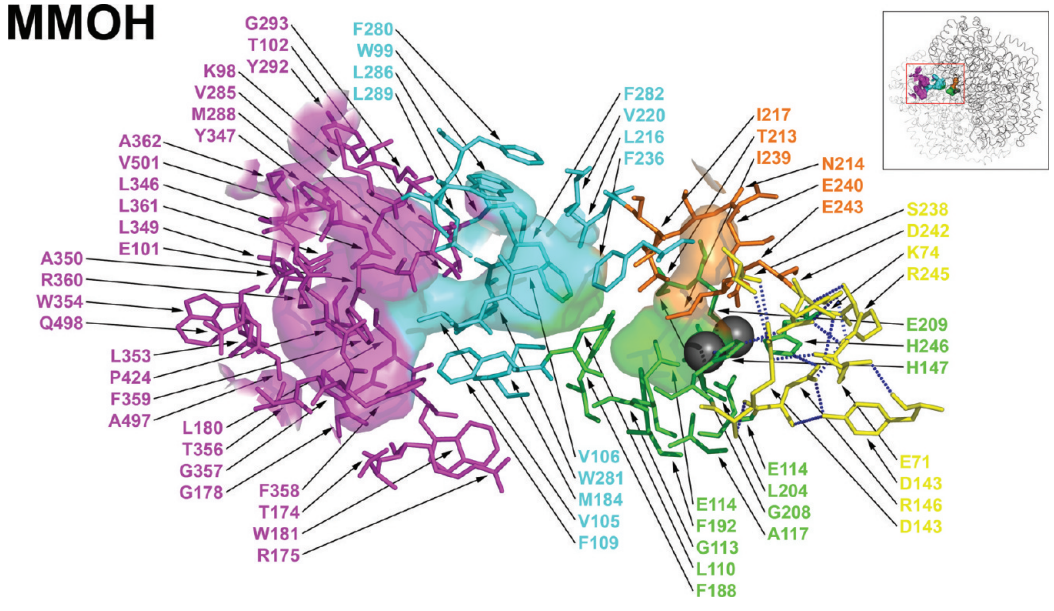

Figure 4. Surface-to-active site pockets in the α-subuint of MMOH. Hydrophobic cavities and pore region pockets are represented as van der Waals surfaces colored magenta (cavity 3), cyan (cavity 2), green (cavity 1), and orange (pore region). Protein residues that contribute to the van der Waals surface are shown as sticks using the same color scheme used for the surface representations. The putative electron-transport hydrogen-bonding network residues are shown as yellow sticks. Iron atoms are represented as dark gray spheres. The inset indicates the orientation of the hydroxylase dimer protomers A (dark ribbons) and B (light ribbons) depicted in the primary figure.

and trajectory in the presence of PHM, and (3) all three determined pathways are conserved among known BMM hydroxylase α-subunit structures. These features are detailed in Figure 7. The substrate access route in PHH with the largest cross section is the pore region, with a diameter of 2.8 Å at its narrowest point near T203, F207, and E233 (Figures 3 and 7A, orange). A pathway through the hydrophobic cavities of PHH charts a second route, which is narrowest at 2.2 Å near P106, H166, and Q113 (Figures 3 and 7A, magenta). This pathway contains the most xenon atoms in the structure of Xe-PHH (vide supra). The third and most constricted path identified in PHH wraps around the protein interior alongside helix E and exits between helices E and H (Figure 7A, gray), tracing a pathway similar to the channel in the ToMOH (Figures 5 and 7D, gray) and T4MOH[13] structures. In the presence of PHM, the trajectories of the pore and channel deviate significantly (Figure 7B). The pore exit opening is almost completely blocked by the regulatory protein where

dx.doi.org/10.1021/bi201248b | *Biochemistry* 2011, 50, 11058–11069

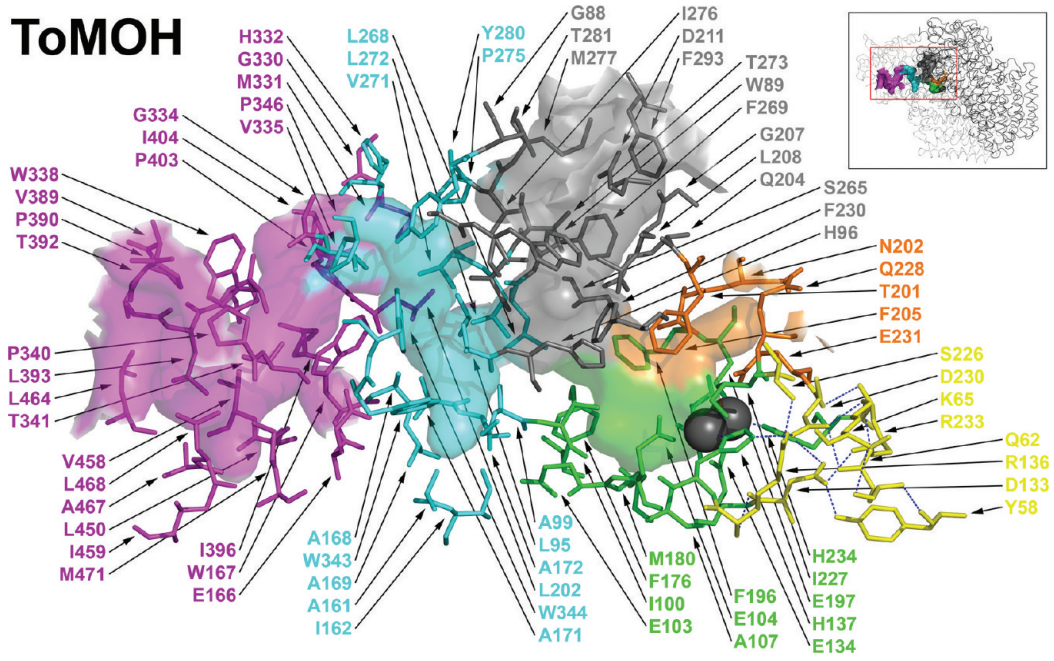

Figure 5. Surface-to-active site pockets in the α-subuint of ToMOH. Hydrophobic cavities, pore region pockets, and channel pockets are represented as van der Waals surfaces colored magenta (cavity 3), cyan (cavity 2), green (cavity 1), orange (pore region), and gray (channel). Protein residues that contribute to the van der Waals surface are shown as sticks using the same color scheme used for the surface representations. The putative electron-transport hydrogen-bonding network residues are shown as yellow sticks. Iron atoms are represented as dark gray spheres. The inset indicates the orientation of the hydroxylase dimer protomers A (dark ribbons) and B (light ribbons) depicted in the primary figure.

bound, causing the calculated trajectory to shift around the four-strand β-sheet of PHM toward the γ-subunit of protomer B to which the regulatory component is bound (Figure 7B, orange). The alteration in this pathway lengthens the pore trajectory by approximately 12 Å but does not expand or contract its narrowest cross section. Noteworthy about the change in this pathway is the fact that the trajectory shift and lengthening begin at the point of the previously noted hydrogen-bonding interaction between residues PHH N204 and PHM S72.[16] The channel trajectory is similarly forced to lengthen, by approximately 10 Å, and shift toward the γ-subunit in the same direction as the pore trajectory (Figure 7B, gray). The effects on both the pore and channel trajectories are exaggerated by the conformational shift in helix F that occurs in conjunction with binding of the regulatory component to the hydroxylase.[16]

Comparing these results to those obtained from a similar analysis of the MMOH (PDB entry 1MTY) and ToMOH (PDB entry 1T0Q) α-subunits reveals additional insight regarding substrate access in BMMs (panels C and D of Figure 7, respectively). Most notably, the pore, hydrophobic cavity, and channel pathways calculated by *CAVER* for PHH are also observed in MMOH and ToMOH. The results indicate that access to the active site by the pathway delineated by a channel in ToMOH,[15] or the open pore in PHH,[16] is not entirely unique to those systems. The relative sizes of each structural feature reveal new similarities and differences between the crystallographically characterized hydroxylases. In both PHH and MMOH, for example, the pore pathway (Figure 7A,C, orange) represents the most accessible route to the active site cavity, whereas the channel pathway (Figure 7A,C, gray) is the most restricted. Accordingly, the MMOH pore pathway is narrowest near E243, E114, and T213, with a diameter of 2.4 Å (Figure 7C, orange). Conversely, the channel in ToMOH (Figure 7D, gray) is the most open pathway observed among all calculated diiron center access routes, with its narrowest cross sectional diameter measuring 3.2 Å, near F293, D211, and M277. The calculated width of the ToMOH channel is considerably larger than that of the analogous channel in PHH (Figure 7A, gray) or MMOH (Figure 7C, gray), the latter of which measures 1.6 Å in diameter at its narrowest dimension, near F290, W308, and W301.

When considering these results from *CAVER*, it is important to remember that the reported cross sectional diameters must be interpreted only as relative values for the respective protein pathways and not as accurate individual measurements. They represent statistical averages for the diameters adopted in the crystalline state of the protein and invariably expand to yield larger cross sections in solution as a result of protein breathing motions. Relevant insights into this breathing phenomenon are provided by computational work on a variety of proteins of differing size, fold, and function, and at different temperatures and under different conditions.[46] Results from this study indicate that, at protein concentrations typical for laboratory solution work and in cellular environments, the interatomic distances that separate secondary structural elements increase by 1.0−1.5 Å as a result of the protein breathing vibrational modes, without perturbing the native fold of the macromolecule or interresidue hydrogen bonds. Because the BMM α-subunits are almost entirely α-helical in secondary structure, it is reasonable to assume on the basis of the theoretical work that the relative cross sectional sizes of the various pockets calculated through *CAVER* analysis are maintained but become considerably larger than the actual numeric values provided.

dx.doi.org/10.1021/bi201248b | *Biochemistry* 2011, 50, 11058−11069

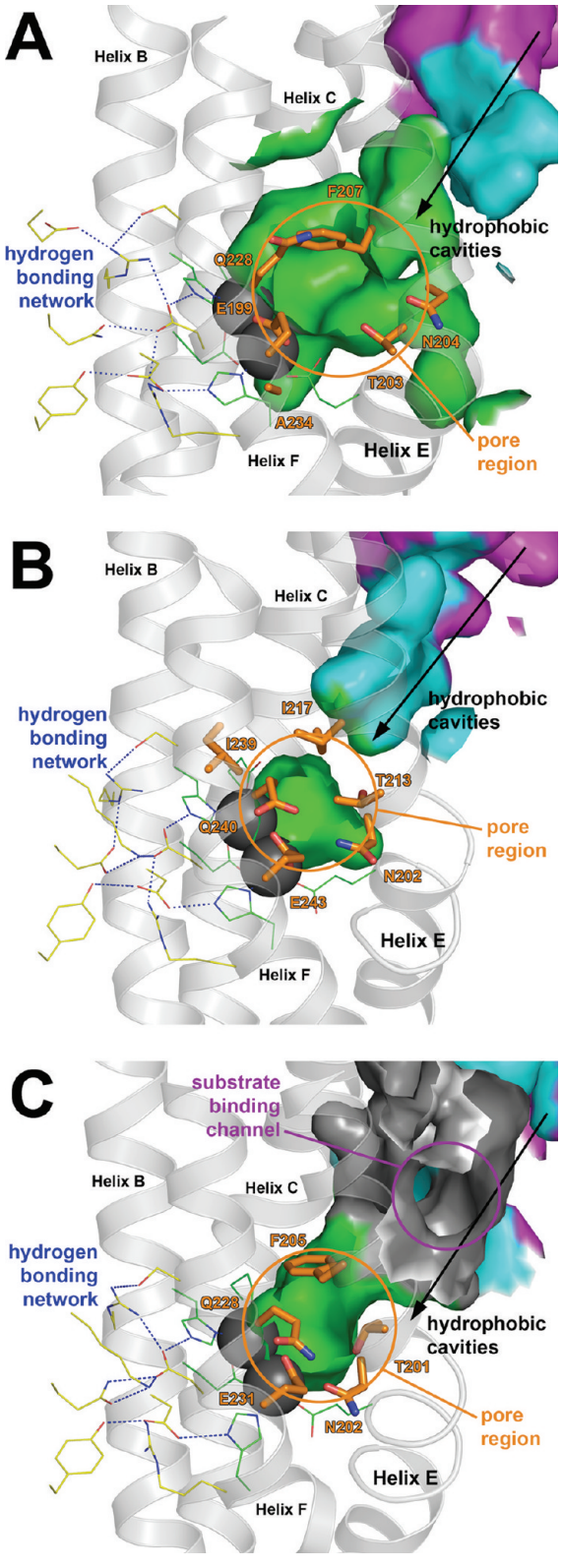

Figure 6. View down the pore pathway into the active site cavity in Xe-PHH (A), MMOH (B), and ToMOH (C). Hydrophobic cavity pockets and the ToMOH channel are represented as van der Waals surfaces colored magenta (cavity 3), cyan (cavity 2), green (cavity 1), and gray (channel). Protein residue side chains that comprise the pore pathway are shown as orange (carbon), blue (nitrogen), and red (oxygen) sticks. The four-helix bundle is represented as light gray ribbons, and iron ligands (green) and the surface-to-diiron center hydrogen-bonding network residues (yellow) are shown as lines.

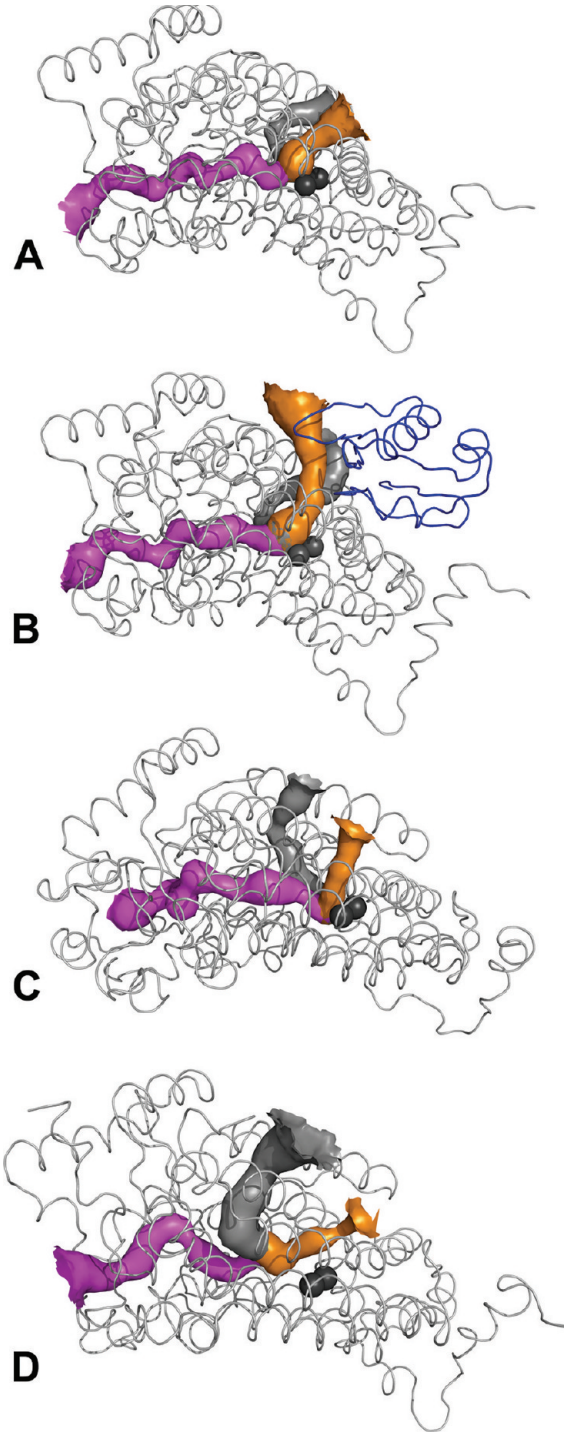

Figure 7. Diiron center access routes in the α-subunit of PHH (A), PHH–PHM (B), MMOH (C), and ToMOH (D) as calculated by *CAVER*. Substrate pathways are represented as magenta (hydrophobic cavities), orange (pore region), and gray (channel) surfaces. The hydroxylase α-subunit is shown as light gray ribbons; PHM is shown as blue ribbons (B only). Iron atoms are shown as dark gray spheres.

■ CONCLUSIONS AND PROSPECTS

Pockets in protein structures usually fall into one of two classes, functional or adventitious, both of which are a consequence of protein fold. Early crystallographic work on MMOH revealed the presence of a series of hydrophobic cavities leading through

dx.doi.org/10.1021/bi201248b | *Biochemistry* 2011, 50, 11058–11069

the α-subunit from the protein surface to the active site pocket.[5] These cavities have since been further examined crystallographically by analyzing product-bound[11] and product analogue-bound[7] structures as well as two Xe-pressurized structures.[10] The results suggested that the hydrophobic cavities in MMOH might constitute the route of methane access to the diiron site during catalysis and are in fact not an adventitious consequence of imperfect folding. The present analysis is perfectly consistent with this conclusion, given the similarities in size and neutrality of CH_4 and O_2. Subsequent structures of ToMOH,[14] T4MOH,[13] and PHH[16] have identified homologous hydrophobic cavities in their respective α-subunit interiors. In contrast to MMOH, however, these structures revealed additional, solvent-exposed molecular access routes to the diiron center: a 40 Å long channel in ToMOH[15] and T4MOH[13] and a 12 Å deep open pore leading to the active site cavity in PHH.[16] ToMOH has also been crystallographically characterized with molecules of bromophenol bound to the interior of its 40 Å long channel, suggesting a possible route of hydrocarbon transport in that system.[15]

The pore in PHH traces the shortest solvent-accessible path to the diiron center in any BMM hydroxylase. Situated directly between the two surface-exposed iron-ligating α-helices and lined with polar residues, the pore is large enough to accommodate one-ring aromatic compounds and may represent the route of active site hydrocarbon access in the PH system.[16] Similar but considerably more constricted porelike regions exist in MMOH,[5] ToMOH,[20] and T4MOH,[13] and these regions vary in size and morphology in the presence of bound product analogues, with the oxidation state of the active site metal ions, or upon formation of the hydroxylase−regulatory protein complex.[7−9,13,14]

Results from this 1.95 Å resolution structure determination of Xe-PHH reveal hydrophobic gas binding sites within a series of highly conserved hydrophobic cavities in the α-subunit. They recapitulate our previous findings about the structure of the PH hydroxylase protein and geometry of the metal-binding sites and provide evidence to support the hypothesis that the conserved hydrophobic cavities in BMM hydroxylases are the route of transport of dioxygen to the catalytic diiron center. Credence for this assignment also derives from the recent structural work on T4MOH and the T4MOH−T4MOD complex, which indicates a closed channel in the hydroxylase−regulatory protein complex but unaltered hydrophobic cavity access, which would allow the system to remain oxygen-saturated for catalysis but simultaneously solvent-limited to maintain the integrity of the active site intermediates required for substrate oxidation.[13] Functional studies of dioxygen activation in ToMOH variants provide additional strong support for the conclusion that O_2 accesses the diiron center through the hydrophobic cavities.[22]

Among the xenon-binding sites observed in PHH, more than 80% are localized entirely within the α-subunit (Figure S1 of the Supporting Information), and 70% of those occur in the hydrophobic cavities, despite the fact that the α-subunit comprises only 54% of the total hydroxylase molecular weight. According to our sequence alignments, the hydrophobicity of a large majority of side chain residues contributing to the xenon-binding sites in the PHH α-subunit are conserved among BMMs (Figure S7 of the Supporting Information). Moreover, the structures of xenon-bound MMOH are similar (Figure S8 of the Supporting Information). These observations strongly implicate the hydrophobic cavities as being a functional rather than a physical consequence of protein folding. The similarities in size, hydrophobicity, and polarizability of xenon and dioxygen (Table S1 of the Supporting Information) suggest that the xenon sites delineate the path of transport of dioxygen to the diiron center during catalysis. This concept extends back to early high-resolution crystallographic studies of small molecule binding in the interior of myoglobin where various small molecules and hydrophobic gases, including the dinitrogen, were found to occupy the same binding sites as xenon.[47] Countless examples of xenon as a crystallographic probe for dioxygen and other small gases binding to protein pockets have subsequently been reported. Relevant examples include xenon as a probe for dioxygen translocation in copper amine oxidase[48] and 3-hydroxybenzoate hydroxylase,[49] and transport of carbon monoxide between the two catalytic sites of a bifunctional carbon monoxide dehydrogenase−acetyl-CoA synthase complex.[50]

If the hydrophobic cavities in BMMs are the route of dioxygen access to the diiron centers, the question of how the three remaining substrates (electrons, protons, and hydrocarbons) access the active site cavities then arises. Considering the level of conservation in the surface-to-diiron center hydrogen-bonding network in the BMM hydroxylase α-subunit, and its similarity to empirically established electron-transport pathways in ribonucleotide reductase R2 subunit[17] and steroyl-acyl carrier protein Δ^9-desaturase,[19] it is probable that electrons reach the diiron center via that network in BMMs as well (Figures 3−6, yellow residues). Similarly, the observation of strictly conserved polar residues and available molecular access pathways in the pore region of the hydroxylase protein structures (Figure 6) leads us to believe that a through-pore route provides for the transfer of a proton from bulk solvent to the diiron center. Additional support for this theory, and consistent with evidence suggesting coupled electron- and proton-transfer events in BMM catalysis,[20] is our previous observation that multiple residues in this region change conformation with the oxidation state of the active site metal ions.[2,4−6,8,9,14] Moreover, recent results from kinetic studies of dioxygen activation in ToMOH T201 variants demonstrate a critical role for the strictly conserved pore threonine residue in proton translocation.[43]

With regard to hydrocarbon substrate and product transport in BMMs other than MMOH, one possibility is that these functions are accomplished using surface-to-active site pathways that are not fully conserved in the α-subunit structures, such as the channel in ToMOH and the open pore in PHH, which provide access routes that are tailored to the substrate preference of the particular hydroxylase. MMOH would not require an additional access pathway because its preferred substrate, CH_4, is a hydrophobic gas like dioxygen and could therefore use the same access pathway. This conclusion is consistent with the fact that all BMMs appear to have evolved from a common ancestor,[3] as well as the notion that the PHH open pore and ToMOH channel pathways were introduced into these BMM hydroxylase α-subunit structures to accommodate their natural aromatic substrates during that evolution. Furthermore, this process may have occurred in exchange for the loss of some oxidizing power in the oxygenated diiron intermediates, perhaps as a result of increased active site solvent exposure, resulting in systems fit to initiate aromatic substrate metabolism but not capable of oxidizing methane as observed in activity and substrate specificity studies of BMMs.[2,20]

These conclusions are consistent with results from our Xe-PHH structure and computational analyses and accordingly provide a more tangible work model for substrate access in BMM hydroxylase structures.

■ ASSOCIATED CONTENT

Supporting Information

Relevant properties of dioxygen, xenon, and methane gas (Table S1), details of the Xe atom-binding sites (Table S2), interatomic distances for xenon and iron atoms (Table S3), views of the hydroxylase dimer (Figure S1), diiron sites (Figure S2) and corresponding composite omit electron density (Figure S3), zinc sites (Figure S4) and corresponding composite omit electron density (Figure S5), extraneous metal-binding sites and corresponding composite omit electron density (Figure S6), BMM hydroxylase α-subunit sequence alignments (Figure S7), and depictions of xenon-binding locations in MMOH form I and II crystal structures (Figure S8). This material is available free of charge via the Internet at http://pubs.acs.org.

Accession Codes

The coordinates and structure factors for xenon-pressurized PHH have been deposited in the Protein Data Bank (entry 3U52).

■ AUTHOR INFORMATION

Corresponding Author

*E-mail: lippard@mit.edu. Telephone: (617) 253-1892. Fax: (617) 258-8150.

Funding

This research was supported by National Institute of General Medical Sciences Grant GM032134 (S.J.L.).

■ ACKNOWLEDGMENTS

We thank Dr. Tzanko Doukov for experimental assistance and Dr. Matthew H. Sazinsky, Dr. Viviana Izzo, and Dr. Christine Tinberg for helpful discussions.

■ REFERENCES

(1) Cafaro, V., Izzo, V., Scognamiglio, R., Notomista, E., Capasso, P., Casbarra, A., Pucci, P., and Di Donato, A. (2004) Phenol Hydroxylase and Toluene/*o*-Xylene Monooxygenase from *Pseudomonas stutzeri* OX1: Interplay between Two Enzymes. *Appl. Environ. Microbiol. 70*, 2211−2219.

(2) Sazinsky, M. H., and Lippard, S. J. (2006) Correlating structure with function in bacterial multicomponent monooxygenases and related diiron proteins. *Acc. Chem. Res. 39*, 558−566.

(3) Leahy, J. G., Batchelor, P. J., and Morcomb, S. M. (2003) Evolution of the soluble diiron monooxygenases. *FEMS Microbiol. Rev. 27*, 449−479.

(4) Rosenzweig, A. C., Brandstetter, H., Whittington, D. A., Nordlund, P., Lippard, S. J., and Frederick, C. A. (1997) Crystal Structures of the Methane Monooxygenase Hydroxylase from *Methylococcus capsulatus* (Bath): Implications for Substrate Gating and Component Interactions. *Proteins 29*, 141−152.

(5) Rosenzweig, A. C., Frederick, C. A., Lippard, S. J., and Nordlund, P. (1993) Crystal structure of a bacterial non-hame iron hydroxylase that catalyzes the biological oxidation of methane. *Nature 366*, 537−543.

(6) Rosenzweig, A. C., Nordlund, P., Takahara, P. M., Frederick, C. A., and Lippard, S. J. (1995) Geometry of the soluble methane monooxygenase catalytic diiron center in two oxidation states. *Chem. Biol. 2*, 409−418.

(7) Sazinsky, M. H., and Lippard, S. J. (2005) Product Bound Structures of the Soluble Methane Monooxygenase Hydroxylase from *Methylococcus capsulatus* (Bath): Protein Motion in the α-Subunit. *J. Am. Chem. Soc. 127*, 5814−5825.

(8) Sazinsky, M. H., Merkx, M., Cadieux, E., Tang, S., and Lippard, S. J. (2004) Preparation and X-ray Structures of Metal-Free, Dicobalt and Dimanganese Forms of Soluble Methane Monooxygenase Hydroxylase from *Methyolococcus capsulatus* (Bath). *Biochemistry 43*, 16263−16276.

(9) Whittington, D. A., and Lippard, S. J. (2001) Crystal Structures of the Soluble Methane Monooxygenase Hydroxylase from *Methylococcus capsulatus* (Bath) Demonstrating Geometrical Variability at the Dinuclear Iron Active Site. *J. Am. Chem. Soc. 123*, 827−838.

(10) Whittington, D. A., Rosenzweig, A. C., Frederick, C. A., and Lippard, S. J. (2001) Xenon and Halogenated Alkanes Track Putative Substrate Binding Cavities in the Soluble Methane Monooxygenase Hydroxylase. *Biochemistry 40*, 3476−3482.

(11) Whittington, D. A., Sazinsky, M. H., and Lippard, S. J. (2001) X-ray Crystal Structure of Alcohol Products Bound at the Active Site of Soluble Methane Monooxygenase Hydroxylase. *J. Am. Chem. Soc. 123*, 1794−1795.

(12) Elango, N., Radhakrishnan, R., Froland, W. A., Wallar, B. J., Earhart, C. A., Lipscomb, J. D., and Ohlendorf, D. H. (1997) Crystal structure of the hydroxylase component of methane monooxygenase from *Methylosinus trichosporium* OB3b. *Protein Sci. 6*, 556−568.

(13) Bailey, L. J., McCoy, J. G., Phillips, G. N. Jr., and Fox, B. G. (2008) Structural Consequences of Effector Protein Complex Formation in a Diiron Hydroxylase. *Proc. Natl. Acad. Sci. U.S.A. 105*, 19194−19198.

(14) McCormick, M. S., Sazinsky, M. H., Condon, K. L., and Lippard, S. J. (2006) X-ray Crystal Structures of Manganese(II)-Reconstituted and Native Toluene/*o*-Xylene Monooxygenase Hydroxylase Reveal Rotamer Shifts in Conserved Residues and an Enhanced View of the Protein Interior. *J. Am. Chem. Soc. 128*, 15108−15110.

(15) Sazinsky, M. H., Bard, J., Di Donato, A., and Lippard, S. J. (2004) Crystal Structure of the Toluene/*o*-Xylene Monooxygenase Hydroxylase from *Pseudomonas stutzeri* OX1: Insight Into the Substrate Specificity, Substrate Channeling, and Active Site Tuning of Multicomponent Monooxygenases. *J. Biol. Chem. 279*, 30600−30610.

(16) Sazinsky, M. H., Dunten, P. W., McCormick, M. S., Di Donato, A., and Lippard, S. J. (2006) X-ray Structure of a Hydroxylase-Regulatory Protein Complex from a Hydrocarbon-Oxidizing Multicomponent Monooxygenase, *Pseudomonas* sp. OX1 Phenol Hydroxylase. *Biochemistry 45*, 15392−15404.

(17) Stubbe, J. (2003) Di-iron-tyrosyl radical ribonucleotide reductases. *Curr. Opin. Chem. Biol. 7*, 183−188.

(18) Carrondo, M. A. (2003) Ferritins, iron uptake and storage from the bacterioferritin viewpoint. *EMBO J. 22*, 1959−1968.

(19) Lindqvist, Y., Huang, W., Schneider, G., and Shanklin, J. (1996) Crystal structure of Δ9D stearoyl-acyl carrier protein desaturase from castor seed and its relationship to other di-iron proteins. *EMBO J. 15*, 4081−4092.

(20) Murray, L. J., and Lippard, S. J. (2007) Substrate Trafficking and Dioxygen Activation in Bacterial Multicomponent Monooxygenases. *Acc. Chem. Res. 40*, 466−474.

(21) McCormick, M. S. (2008) Structural Investigations of Hydroxylase Proteins and Complexes in Bacterial Multicomponent Monooxygenase Systems. Ph.D. Thesis, Massachusetts Institute of Technology, Cambridge, MA.

(22) Song, W. J., Gucinski, G., Sazinsky, M. H., and Lippard, S. J. (2011) Tracking a Defined Route for O_2 Migration in a Dioxygen-Activating Diiron Enzyme. *Proc. Natl. Acad. Sci. U.S.A. 108*, 14795−14800.

(23) Schoenborn, B. P., Watson, H. C., and Kendrew, J. C. (1965) Binding of Xenon to Sperm Whale Myoglobin. *Nature 207*, 28−30.

(24) DeLano, W. L. (2002) *The PyMOL Molecular Graphics System*, DeLano Scientific, San Carlos, CA.

(25) Petrek, M., Otyepka, M., Banás, P., Kosinová, P., Koca, J., and Damborský, J. (2006) *CAVER*: A new tool to explore routes from protein clefts, pockets and cavities. *BMC Bioinf. 7*, 316−324.
(26) Gibbs, C. R. (1976) Characterization and Application of FerroZine Iron Reagent as a Ferrous Iron Indicator. *Anal. Chem. 48*, 1197−1201.
(27) Tinberg, C. T., Song, W. J., Izzo, V., and Lippard, S. J. (2011) Multiple Roles of Component Proteins in Bacterial Multicomponent Monooxygenases: Phenol Hydroxylase and Toluene/o-Xylene Monooxygenase from *Pseudomonas* sp. OX1. *Biochemistry 50*, 1788−1798.
(28) Soltis, S. M., Stowell, M. H. B., Wiener, M. C., Phillips, G. N. Jr., and Rees, D. C. (1997) Successful flash-cooling of xenon-derivatized myoglobin crystals. *J. Appl. Crystallogr. 30*, 190−194.
(29) Cohen, A. E., Ellis, P. J., Miller, M. D., Deacon, A. M., and Phizackerley, R. P. (2002) An automated system to mount cryo-cooled protein crystals on a synchrotron beamline, using compact sample cassettes and a small-scale robot. *J. Appl. Crystallogr. 35*, 720−726.
(30) McPhillips, T. M., McPhillips, S. E., Chiu, H. J., Cohen, A. E., Deacon, A. M., Ellis, P. J., Garman, E., Gonzalez, A., Sauter, N. K., Phizackerley, R. P., Soltis, S. M., and Kuhn, P. (2002) *Blu-Ice* and the *Distributed Control System*: Software for data acquisition and instrument control at macromolecular crystallography beamlines. *J. Synchrotron Radiat. 9*, 401−406.
(31) Otwinowski, Z., and Minor, W. (1997) Processing of X-Ray Diffraction Data Collected in Oscillation Mode. *Methods Enzymol. 276*, 307−326.
(32) Kissinger, C. R., Gehlhaar, D. K., and Fogel, D. B. (1999) Rapid automated molecular replacement by evolutionary search. *Acta Crystallogr. D55*, 484−491.
(33) Emsley, P., and Cowtan, K. (2004) *Coot*: Model-building tools for molecular graphics. *Acta Crystallogr. D60*, 2126−2132.
(34) Murshudov, G. N., Vagin, A. A., and Dodson, E. J. (1997) Refinement of Macromolecular Structures by the Maximum-Likelihood Method. *Acta Crystallogr. D53*, 240−255.
(35) Collaborative Computational Project, Number 4 (1994) The *CCP4* suite: Programs for Protein Crystallography. *Acta Crystallogr. D50*, 760−763.
(36) Brunger, A. T., Adams, P. D., Clore, G. M., DeLano, W. L., Gros, P., Grosse-Kunstleve, R. W., Jiang, J.-S., Kuszewski, J., Nilges, M., Pannu, N. S., Read, R. J., Rice, L. M., Simonson, T., and Warren, G. L. (1998) *Crystallography & NMR System*: A New Software Suite for Macromolecular Structure Determination. *Acta Crystallogr. D54*, 905−921.
(37) Kleywegt, G. J., and Jones, T. A. (1998) Databases in Protein Crystallography. *Acta Crystallogr. D54*, 1119−1131.
(38) Larkin, M. A., Blackshields, G., Brown, N. P., Chenna, R., McGettigan, P. A., McWilliam, H., Valentin, F., Wallace, I. M., Wilm, A., Lopez, R., Thompson, J. D., Gibson, T. J., and Higgins, D. G. (2007) Clustal W and Clustal X version 2.0. *Bioinformatics 23*, 2947−2948.
(39) Gassner, G. T., and Lippard, S. J. (1999) Component interactions in the soluble methane monooxygenase system from *Methylococcus capsulatus* (Bath). *Biochemistry 38*, 12768−12785.
(40) Liang, H.-C., Kim, E., Incarvito, C. D., Rheingold, A. L., and Karlin, K. D. (2002) A Bis-Acetonitrile Two-Coordinate Copper(I) Complex: Synthesis and Characterization of Highly Soluble $B(C_6F_5)_4^-$ Salts of $[Cu(MeCN)_2]^+$ and $[Cu(MeCN)_4]$. *Inorg. Chem. 41*, 2209−2212.
(41) Sanyal, I., Strange, R. W., Blackburn, N. J., and Karlin, K. D. (1991) Formation of a copper-dioxygen complex (Cu_2-O_2) using simple imidazole ligands. *J. Am. Chem. Soc. 113*, 4692−4693.
(42) Prangé, T., Schiltz, M., Pernot, L., Colloc'h, N., Longhi, S., Bourguet, W., and Fourme, R. (1998) Exploring Hydrophobic Sites in Proteins with Xenon or Krypton. *Proteins 30*, 61−73.
(43) Song, W. J., McCormick, M. S., Behan, R. K., Sazinsky, M. H., Jiang, W., Lin, J., Krebs, C., and Lippard, S. J. (2010) Active Site Threonine Facilitates Proton Transfer during Dioxygen Activation at the Diiron Center of Toluene/*o*-Xylene Monooxygenase Hydroxylase. *J. Am. Chem. Soc. 132*, 13582−13585.
(44) Lee, S.-K., and Lipscomb, J. D. (1999) Oxygen Activation Catalyzed by Methane Monooxygenase Hydroxylase Component: Proton Delivery during the O-O Bond Cleavage Steps. *Biochemistry 38*, 4423−4432.
(45) Tinberg, C. E., and Lippard, S. J. (2009) Revisiting the Mechanism of Dioxygen Activation in Soluble Methane Monooxygenase from *M. capsulatus* (Bath): Evidence for a Multi-Step, Proton-Dependent Reaction Pathway. *Biochemistry 48*, 12145−12158.
(46) Makowski, L., Rodi, D. J., Mandava, S., Minh, D. D. L., Gore, D. B., and Fischetti, R. F. (2008) Molecular Crowding Inhibits Intramolecular Breathing Motions in Proteins. *J. Mol. Biol. 375*, 529−546.
(47) Tilton, R. F. Jr., and Petsko, G. A. (1988) A structure of sperm whale myoglobin at a nitrogen gas pressure of 145 atm. *Biochemistry 27*, 6574−6582.
(48) Johnson, B. J., Cohen, J., Welford, R. W., Pearson, A. R., Schulten, K., Klinman, J. P., and Wilmot, C. M. (2007) Exploring Molecular Oxygen Pathways in *Hansenula polymorpha* Copper-containing Amine Oxidase. *J. Biol. Chem. 282*, 17767−17776.
(49) Schiltz, M., Fourme, R., Broutin, I., and Prangé, T. (1995) The catalytic site of serine proteinases as a specific binding cavity for xenon. *Structure 3*, 309−316.
(50) Doukov, T. I., Blasiak, L. C., Seravalli, J., Ragsdale, S. W., and Drennan, C. L. (2008) Xenon in and at the End of the Tunnel of Bifunctional Carbon Monoxide Dehydrogenase/Acetyl-CoA Synthase. *Biochemistry 47*, 3474−3483.